Available online at www.sciencedirect.com
ScienceDirect
Computers & Fluids 37 (2008) 1238–1252
computers & fluids
www.elsevier.com/locate/compfluid

An applicability study of advanced lattice-Boltzmann techniques for moving, no-slip boundaries and local grid refinement

M. Rohde [a,*], J.J. Derksen [b], H.E.A. Van den Akker [b]

[a] Delft University of Technology, Physics of Nuclear Reactors, Mekelweg 15, 2629 JB, Delft, The Netherlands
[b] Delft University of Technology, Multi-Scale Physics, The Netherlands

Received 16 July 2006; received in revised form 2 March 2007; accepted 4 October 2007
Available online 14 December 2007

Abstract

In this paper, two previously proposed lattice-Boltzmann techniques for no-slip boundaries and local grid refinement have been studied with the help of existing experimental and numerical data on a sedimenting sphere in a tank. These data comprise flow characteristics as well as the sedimentation trajectory and velocity of the sphere. It was found that the methods are capable of accurately describing the experimentally obtained data and show stable behaviour, even for solid-to-fluid density ratios close to one. Moreover, the proposed no-slip boundary methods produce more accurate results than the adaptive forcing technique.

1. Introduction

Compared to computational fluid dynamics (CFD) methods based on finite volume and finite difference/elements techniques, the lattice-Boltzmann method (LBM) is a relatively new method to simulate fluid flow. Instead of considering the fluid as a large set of fluid packages acting on each other (in terms of momentum and mass transport), fluid flow in LBM is described by the microscopic transport and collisions of fluid particles according to the discretized Boltzmann equation.

Due to the effort of a large number of authors, the method has reached a certain maturity. In the field of large industrial scale applications, however, only a few references can be found [5–9]. Due to the large range of scales in such applications, one needs to apply local grid refinement techniques and no-slip boundary schemes that do not lower the accuracy of the calculations. For this reason, new lattice-Boltzmann techniques for local grid refinement [3,10–16] and accurate (moving) no-slip boundaries [1,2,17–21] have been developed by a number of researchers that enlarge the scope of applications such as particle suspensions [22–25] and industrial applications [5,6].

The main objectives of this paper are (i) to investigate the applicability of the volumetric lattice-Boltzmann techniques for no-slip boundaries as presented in Refs. [1,2] and the local grid refinement technique as presented in Ref. [3] and (ii) to compare the effect of using two different techniques for moving boundaries as described in Refs. [1,2,5]. We thereby will use the case of a sedimenting sphere in a tank, which is a transient flow problem that comprises a *freely* moving boundary and in which a variety of scales exist.

The case of a sedimenting sphere in a box has been used by a number of researchers to study the applicability of advanced lattice-Boltzmann techniques (see e.g. Refs. [4,21,26,27]). In this work, we will use the results of ten Cate et al. [4], who both experimentally and numerically studied this problem at relatively low Reynolds numbers. Sedimentation velocity of the sphere, as well as details from the flow field will be used to examine the capabilities of the different lattice-Boltzmann techniques.

* Corresponding author.
E-mail address: m.rohde@tudelft.nl (M. Rohde).
URL: http://www.rrr.tudelft.nl/pnr/ (M. Rohde).

0045-7930/$ - see front matter © 2007 Elsevier Ltd. All rights reserved.
doi:10.1016/j.compfluid.2007.10.012

Nomenclature

A^α	surface of a facet (ls^2)
$\vec{c}_i$	lattice velocity in direction i (ls lt^{-1})
C	computational effort (–)
D	diameter of a smooth (i.e. real) sphere (ls)
D_{geom}	outer diameter of a triangulated sphere (ls)
D_{hydr}	hydrodynamical sphere diameter(ls)
E_μ	exp. uncertainty due to viscosity (–)
E_s	exp. uncertainty due to sphere position (–)
$\vec{F}_{\text{buoyancy}}$	Buoyancy force acting on the sphere (ls lt^{-2})
$\vec{F}_{\text{fp}}$	Hydrodynamic force acting on the sphere (ls lt^{-2})
$\vec{F}_g$	gravitational force (ls lt^{-2})
$\vec{F}^\alpha$	hydrodynamic force acting on facet S^α (ls lt^{-2})
$\vec{g}$	gravitational acceleration (ls lt^{-2})
G_n	grid number n
H_{G_n}	specific size of the embedded grid G_n (ls)
I	moment of inertia (ls^2)
L_{G_n}	specific size of the embedded grid G_n (ls)
L_x, L_y, L_z	size of the tank in each spatial direction ls
M	mass of the sphere (–)
Ma	Mach number (–)
n	level of refinement (–)
$\vec{n}^\alpha$	normal vector of facet α (–)
N_i	local mass distribution (ls^{-3})
$\vec{r}_\alpha$	vector between center of sphere and center of facet S^α (ls)
Re_∞	Reynolds number ($= W_\infty D/\nu$) (–)
S	spatial rescaling factor (m ls^{-1})
T	temporal rescaling factor (s lt^{-1})
$\vec{T}_p$	torque acting on the sphere (ls^2 lt^{-2})
Δt	discrete time step (lt)
$\vec{x}$	spatial position (ls)
$\vec{x}_{G_n,0}$	position of the embedded grid G_n(ls)
Δx, Δy, Δz	grid spacing in each spatial direction (ls)
$\vec{u}$	velocity (u_x, u_y, u_z) or (u, v, w) (ls lt^{-1})
$\vec{u}_b$	velocity of the no-slip boundary (ls lt^{-1})
ΔV	volume of a cubic grid cell (ls^3)
W	sedimentation velocity of the sphere (ls lt^{-1})
W_∞	steady-state sedimentation velocity of the sphere in an infinite medium (ls lt^{-1})
z_0	initial position of the sphere for simulations S1–S6 (ls)
z_1	Initial position of the sphere for simulation S7 (ls)

Greek symbols

$\Gamma_i^{\text{in},\alpha}$	mass hitting facet S^α (–)
$\Gamma_i^{\text{out},\alpha}$	Mass reflected from facet S^α (–)
δ	gap size (ls)
δ_∞	measured gap when the sphere touches the bottom (ls)
Δ_f	average size of the facets (ls)
ν	kinematic viscosity (ls^2 lt^{-1})
ρ_f	fluid density (ls^{-3})
ρ_s	density of the sphere (ls^{-3})
Ω_i	collision operator in direction i (–)
ls	lattice spacing (spatial lattice-Boltzmann unit)
lt	lattice time step (temporal lattice-Boltzmann unit)

2. A sedimenting sphere in a tank

The tank consists of four vertical walls and a square bottom and contains a fluid of a specific viscosity and density. The sphere is released near the top of the tank above the center of the bottom. Due to the density difference of the sphere and the fluid, the sphere starts to sediment, until it reaches the bottom of the tank. The setup is schematically shown in Fig. 1.

The sedimentation trajectory of the sphere consists of three different stages. First, the sphere starts to accelerate until the buoyancy force, the gravitational force and the drag all acting on the sphere balance. Consequently, a steady-state sedimentation velocity is reached. Finally, as the sphere approaches the bottom of the tank, it decelerates due to the forces induced by the fluid being squeezed out of the decreasing gap.

In the next section, we will briefly recapitulate the results of ten Cate et al. We will then continue with our lattice-Boltzmann simulations and compare the results with the results as found by ten Cate et al.

2.1. Work of ten Cate et al.

In the experiments, a small spherical Nylon ball was released at height z_0 in a tank filled with silicone oil (z_0

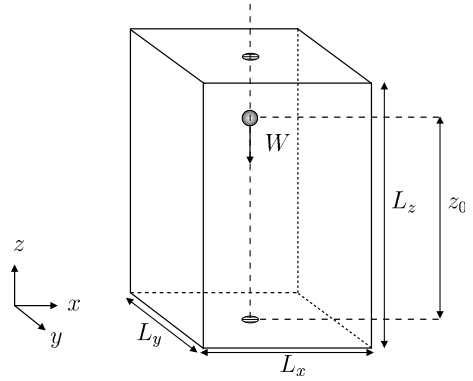

Fig. 1. Schematic representation of a sedimenting sphere in a tank. The size of the tank is denoted by L_x, L_y and L_z and the sedimentation velocity by W.

refers to the distance between the bottom of the tank and the center of the ball). The velocity field in a vertical cross-section of the tank was obtained by performing particle imaging velocimetry (PIV) measurements. From these measurements, also the position and sedimentation velocity of the ball were derived, thereby using several image processing techniques. By varying the type of silicone oil (and thus the viscosity and density of the fluid), measurements could be performed at four Reynolds numbers, viz. $Re_\infty = 1.5, 4.1, 11.6$ and 31.9. The Reynolds number in Ref. [4] was defined as $Re_\infty \equiv W_\infty D/v$, with W_∞ denoting the steady-state sedimentation velocity of a single sphere in an infinite medium and D the sphere's diameter.

The simulations in Ref. [4] were performed by means of the lattice-Boltzmann method. Although the spatial and temporal resolution were varied, a *uniform* grid was implemented. The lattice-Boltzmann scheme used was that of Somers [28] (being an 18-speed single-relaxation scheme with dampened higher-order terms) and the no-slip boundary at the surface of the moving sphere was imposed by the adaptive forcing technique [5]. The free surface of the fluid and the walls of the tank were treated as no-slip boundaries, thereby using the half-way bounce-back method. For the trajectory of the sphere closely above the bottom, a model for the lubrication force [29] was implemented to account for the lack of resolution in the gap between the sphere and the bottom of the tank for gap sizes smaller than one grid spacing.

As the adaptive forcing technique requires fluid nodes *inside* the sphere, instabilities may occur while solving the equation of motion for solid-to-fluid density ratios close to 1 [30]. The density ratios in the experiments were therefore kept larger than 1.15. Moreover, the forces involved needed to be averaged over two time steps to suppress instabilities.

In general, the simulations agreed reasonably well with the experiments for all Reynolds numbers considered. The largest deviation in the maximum sedimentation velocity with respect to the experimental findings amounted to 5% at $Re_\infty = 1.5$, while for the higher Reynolds numbers a deviation smaller than 1% was found. The sedimentation velocity showed a wiggly behaviour, possibly due to the adaptive forcing method applied. Time series of the streamwise fluid velocity at a specific location in the tank showed a clear deviation with the experiments at $Re_\infty = 1.5$. Increasing the resolution improved the simulation results. Regarding the sedimentation velocity and position of the sphere near the bottom of the tank, the measurements and (modelled) sedimentation velocity agreed reasonably well.

3. Brief description of the applied lattice-Boltzmann methods

3.1. Volumetric boundary technique for moving no-slip walls

The lattice-Boltzmann method originally is a finite difference discretization scheme [31]. It can, however, also be interpreted as a *volumetric* scheme,

$$N_i(\vec{x} + \vec{c}_i\Delta t, t + \Delta t) = N_i(\vec{x}, t) + \Omega_i(N(\vec{x}, t)). \tag{1}$$

where the masses N_i are uniformly distributed throughout a cubic cell with center $\vec{x}$ and volume $\Delta V = \Delta x \times \Delta y \times \Delta z$. For the non-cubic cells in the vicinity of a solid surface, Chen et al. [32] proposed a modified bounce-back scheme, which consists of the following steps: (i) mass in the cells adjacent to the surface (i.e. *boundary cells*) hits the surface of an object, (ii) this mass is reflected (i.e. bounced back) in the opposite direction and (iii) is redistributed throughout the surrounding cells. Such a process can be described by

$$N_i(\vec{x} + \vec{c}_i\Delta t, t + \Delta t) = P_i^{\text{undist}}(\vec{x})N_i'(\vec{x}, t) + Q_i(\vec{x} + \vec{c}_i\Delta t, t), \tag{2}$$

where $N_i'(\vec{x}, t) \equiv N_i(\vec{x}, t) + \Omega_i(\vec{x}, t)$ is the right-hand side of the lattice-Boltzmann scheme for a cubic cells and $P_i^{\text{undist}}(\vec{x})$ represents the fraction of mass that does not hit the surface during the propagation step. The term $Q_i(\vec{x} + \vec{c}_i\Delta t, t)$ represents the reflected mass arriving in cell $\vec{x} + \vec{c}_i\Delta t$.

This method was extended to moving boundaries by Rohde et al. [1], analogous to Ladd's approach for moving staircase shaped surfaces [17],

$$N_i(\vec{x} + \vec{c}_i\Delta t, t_*) = P_i^{\text{undist}}(\vec{x})N_i'(\vec{x}, t) + Q_i(\vec{x} + \vec{c}_i\Delta t, t) + B_i(\vec{x} + \vec{c}_i\Delta t, t), \tag{3}$$

with $B_i(\vec{x} + \vec{c}_i\Delta t, t)$ being the volume-weighed, additional mass representing the extra momentum gained due to the moving surface.

It should be noted that, although the accuracy of the calculations is increased due to the more detailed description of the no-slip surface, a non-physical dependency on the viscosity exists [33]. This is an intrinsic property of the combination of the bounce-back principle and the model for the non-equilibrium distribution (e.g. the Lattice Bhatnagar-Gross-Krook (LBGK) scheme or the multiple relaxation times (MRT) scheme [34]). Ginzburg and d'Humières [20] and Pan et al. [35] showed that using the MRT scheme together with the Multi-Reflection boundary technique [20] significantly reduces this unwanted viscosity effect.

3.2. Adaptive forcing technique

In the adaptive forcing technique, the fluid velocity *on* the moving boundary (obtained from interpolating velocities of neighbouring grid nodes) is adjusted by applying a local force each time step [5]. By doing so, the prescribed wall velocity can be imposed on the fluid. First, the deviation in the wall velocity $\delta\vec{u}_b$ is calculated from the prescribed wall velocity and the second-order interpolation of the flow velocities at the grid nodes. Then, forces are applied to the same neighbouring grid nodes,

$$f_k^n = R_1 f_k^{n-1} + R_2 \sum_j G_k(\vec{r}_j^n)(\delta\vec{u}_b)_j^n, \tag{4}$$

with n denoting discrete time, k and j denoting the location of the neighbouring grid nodes and G_k denoting the interpolation coefficients. The R_1 and R_2 are empirically determined parameters and are set to 0.95 and 1.8, respectively. The accuracy of the algorithm is improved by iterating Eq. (4) a few times per time step.

3.3. Local grid refinement technique

The technique as described in Ref. [3] can be considered as a member of a class of methods that use *locally embedded uniform grids*. These techniques use patches of refined, uniform grids, superimposed on the main coarse grid. On top of that, time is also discretized such that $\Delta x/\Delta t = 1$ on each grid, ensuring that the standard lattice-Boltzmann equation can be used on each grid.

The proposed method is different from other locally embedded uniform grid techniques in the way particle distributions propagate from one grid to another. In most methods [10–12], particle distributions are treated as densities residing on grid nodes, and are interpolated (in time and space) and re-scaled on the nodes shared by both grids subsequently. In our method, the particles are considered as mass, propagating from coarse grid cells to fine grid cells and vice versa. In this way, mass conservation is imposed. Moreover, no adjustment is required considering the non-equilibrium distribution, which makes this method applicable to any lattice-Boltzmann scheme for cubic lattice configurations (e.g. the scheme of Somers et al. [28] and the multiple relaxation time method [34]). The steps of the method are as follows:

Step 1. Collision step on the coarse and the fine grid cells.
Step 2. Homogeneous redistribution of mass from the coarse grid cells (adjacent to the fine grid) to $n^{\mathscr{D}}$ fine grid cells ($\mathscr{D}$ is the number of spatial dimensions and n is the level of refinement).
Step 3. Propagation step on the fine grid, including the fine grid cells that overlap the coarse grid.
Step 4. (Repeat $n-1$ times):
  Step 4a. Collision step on the fine grid (excluding the fine grid cells that overlap the coarse grid).
  Step 4b. Same as step 3.
Step 5. Homogeneous redistribution of particle densities from fine grid cells (which overlap the coarse grid cells adjacent to the fine grid) to these coarse grid cells.

The details of the method can be found in Ref. [3].

4. Description of the simulations

The series of simulations performed can be split into two categories. The first category refers to simulations of the main part of the sedimentation trajectory at all Reynolds numbers studied in Ref. [4]. The second category comprises one single simulation at $Re_\infty = 1.5$ only, and refers to the situation in which the sphere is close to the bottom of the tank.

4.1. Main part of the trajectory (simulations S1–S6)

Simulations S1–S4 refer to the sedimentation experiments for the four Reynolds numbers as described in Ref. [4]. In simulation S5, a low solid-to-fluid density ratio is used for $Re_\infty = 1.5$. In simulation S6, the effect of using interpolation in the volumetric technique for moving no-slip boundaries is studied [2].

For the simulations of the main part of the trajectory, two different resolutions are used; a coarse grid for the larger part of the tank and a fine grid covering the sedimentation trajectory of the sphere (see Fig. 2). Since the diameter of the sphere is chosen to be $D \approx 9$ (ls) for all simulations (which is as close as possible to the diameter $D \approx 8$, used in Ref. [4] in order to obtain a meaningful comparison), we define the size L_{G_0} to be 16 (ls), so that the region with highest velocity gradients is covered. The computational effort is now reduced by roughly 90% compared to the uniform grid simulation carried out by ten Cate et al.

The parameters of the simulations S1–S6 are chosen in such a way that the maximum possible sphere velocity is approximately $w = W_\infty \approx 3 \times 10^{-2}$, resulting in a Mach number being much smaller than 1 ($Ma \sim 0.05$) for the 19-speed LBGK scheme used in the simulations. The settings can be found in Table 1.

The moving boundary of the sphere is imposed by the volumetric technique as described in Ref. [1]. In addition, we apply the volumetric interpolation technique as described in Ref. [2]. The latter technique possibly favours the accuracy of the simulations, as was shown in Ref. [2] for the case of Poiseuille flow in an skew channel: although the *order* of accuracy was not reduced by applying the interpolation, the numerical error was.

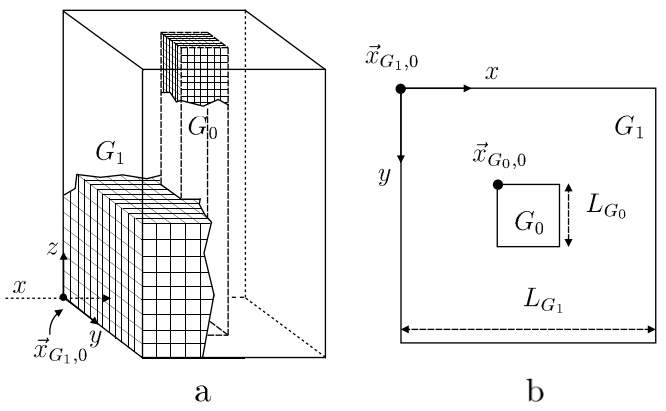

Fig. 2. Grid setup for the main trajectory of a sphere in a tank (a) 3D view and (b) bottom plane. G_0 refers to the fine grid, G_1 to the coarse grid. The base of each grid is square, hence the size of the base is denoted by L_{G_n}. The position of each grid with respect to the domain is defined with the point $\vec{x}_{G_n,0}$.

Table 1
Simulation settings for the main part of the sedimentation trajectory of a sphere in a tank

	S1	S2	S3	S4	S5	S6
Re_∞	1.5	4.1	11.6	31.9	1.5	1.5
ν	$\frac{1}{6}$	$\frac{1}{12}$	$\frac{3}{100}$	$\frac{1}{100}$	$\frac{1}{6}$	$\frac{1}{6}$
$W_\infty(\times 10^{-2})$	−2.736	−3.688	−3.667	−2.736	−2.736	−2.736
$g_z(\times 10^{-3})$	8.445	6.004	2.511	0.9480	130.6	8.454
D_{hydr}	9.032	9.258	9.510	9.854	9.032	9.027
$L_x \times L_y \times L_z$	$60 \times 60 \times 96$	$62 \times 62 \times 98$	$64 \times 64 \times 100$	$66 \times 66 \times 106$	$60 \times 60 \times 96$	$60 \times 60 \times 96$
z_0	78.27	80.23	82.42	85.40	78.27	78.24
L_{G_o}	16	16	16	16	16	16
L_{G_1}	60	62	64	66	60	60
$\vec{x}_{G_0,0}$	(22, 22, 0)	(22, 22, 0)	(24, 24, 0)	(26, 26, 0)	(22, 22, 0)	(22, 22, 0)
$\vec{x}_{G_1,0}$	(0, 0, 0)	(0, 0, 0)	(0, 0, 0)	(0, 0, 0)	(0, 0, 0)	(0, 0, 0)
$S(\times 10^{-3})$	1.661	1.620	1.577	1.522	1.661	1.662
$T(\times 10^{-4})$	11.96	9.958	6.355	3.836	11.96	11.97
ρ_s/ρ_f	1.155	1.161	1.164	1.167	1.010	1.155
Ma	0.0474	0.0639	0.0635	0.0474	0.0474	0.0474

All quantities are written in *fine* lattice units.

The discretized sphere consists of 176 triangular facets, each facet having a side-length of roughly $\Delta_f \approx 2$ (ls). The total surface of all facets, being the surface of the discretized sphere, is equal to the surface of a perfect sphere with a diameter $D = 9$ (ls). This implies that the distance connecting the center of the sphere and the corner points of the facets, being the *geometrical diameter*, amounts to approximately $D_{\text{geom}} \approx 9.16$ (ls). The hydrodynamic diameter D_{hydr}, which is unphysically dependent on the viscosity (see e.g. [17]), differs per simulation. Table 1 shows the hydrodynamic diameter for each case, which is determined by using Hasimoto's analytic expression for the drag on a regular array of spheres in the Stokes regime [1,36]. Note that by doing so, an unknown uncertainty regarding the hydrodynamic diameter is introduced, since the flow problem studied here differs from the flow in an array of spheres and Hasimoto's expression is meant for Stokes flow.

For the vertical walls and the bottom of the tank, all being no-slip boundaries, the simple-to-implement half-way Bounce-Back method is applied. This implies that the size of the tank cannot be set exactly to the size used in the experiments in Ref. [4], since the position of the wall is also determined by the viscosity as well as the flow characteristics when using the half-way Bounce-Back method [33]. The influence on the results, however, is found to be very small. Simulations at $Re_\infty = 11.6$ revealed that the sedimentation velocity of the sphere hardly changes ($\ll 1\%$) when a tank of $62 \times 62 \times 102$ (ls^3) is used instead of a tank of $64 \times 64 \times 100$ (ls^3) (results not shown here). For the top of the tank, where the silicone oil is in contact with air, the free-slip boundary condition is used.

Although we expect the simulated sedimentation velocity to become less accurate (and even unphysical) as the gap size between the sphere and the bottom of the tank is roughly 1–2 (ls), the simulations will be continued until the sphere hits the bottom. Special attention should then be taken to the treatment of both the no-slip boundary at the bottom of the tank and the bottom side of the moving sphere, since boundary techniques may interfere with each other in the gap. For the bottom of the tank, the half-way bounce-back rule can still be applied, even for gap sizes less than one grid spacing. On the contrary, the volumetric boundary technique with interpolation can only be used for gap sizes larger than 1 (ls), since two points are needed for the interpolation. Hence, for smaller gap sizes, the uniform redistribution is applied (see Fig. 3).

Table 1 shows that in the case of simulations S2 and S4, grid G_0 is not exactly positioned in the center of the tank. Such an asymmetric grid setup could possibly lead to a lateral motion of the sphere. Tests revealed, however, that this is not the case. The maximum lateral displacement was found for simulation S4, and amounted to +0.1 (ls) for both the x- and y-directions.

As the sphere is freely moving through the fluid now, its transient motion is determined by the gravitational force $\vec{F}_g$ and the total hydrodynamic force $\vec{F}_{fp}$ acting on the surface of the sphere (the latter consists of the buoyancy force, the drag, the added mass force and the history forces). The sphere may rotate and as a result, each facet α has its own equation of motion, which is

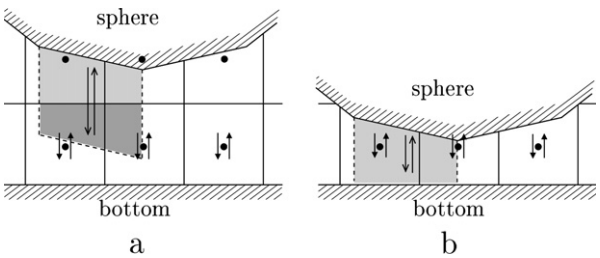

Fig. 3. Treatment of the bottom and sphere no-slip boundaries for gap sizes (a) larger than 1 (ls) and (b) smaller than 1 (ls). Different arrow heads are used to make a distinction between the bounce-back process regarding the sphere boundary (open arrows) and the bottom (closed arrows). The two grey colors in (a) indicate the two areas that are used for the interpolation of particle densities, in analogy with [1]. In (b), such an arrangement of two separate areas is not possible.

$$\frac{\mathrm{d}\vec{u}_\alpha}{\mathrm{d}t} = \frac{\vec{F}_{\mathrm{fp}}}{M} + \frac{\vec{F}_{\mathrm{g}}}{M} + \frac{\vec{T}_{\mathrm{p}}}{I} \times \vec{r}_\alpha, \tag{5}$$

with M being the mass of the sphere, $I = \frac{1}{10} M D_{\mathrm{hydr}}^2$ denoting the moment of inertia, $\vec{T}_{\mathrm{p}}$ being the torque acting on the sphere and $\vec{r}_\alpha$ being the vector between the center of mass and the center of a facet α. The hydrodynamic force and the torque acting on the sphere are

$$\vec{F}_{\mathrm{fp}} = \vec{F}_{\mathrm{buoyancy}} + \sum_\alpha \vec{F}_\alpha$$

$$\vec{T}_{\mathrm{p}} = \sum_\alpha \vec{r} \times \vec{F}_\alpha$$

thereby using

$$\vec{F}^\alpha = \frac{1}{\Delta t A^\alpha} \left[\sum_{i \in c_i \cdot \vec{n}^\alpha \leqslant 0} \vec{c}_i \Gamma_i^{\mathrm{in},\alpha} - \sum_{i \in c_i \cdot \vec{n}^\alpha > 0} \vec{c}_i \left(\Gamma_i^{\mathrm{out},\alpha} + \Delta \Gamma_i^{\mathrm{out},\alpha} \right) \right]$$

for the hydrodynamic force acting on each separate facet [3]. Note that the buoyancy force is explicitly imposed here by using

$$\vec{F}_{\mathrm{buoyancy}} = -\frac{1}{6} \rho_{\mathrm{f}} \vec{g} \pi D_{\mathrm{hydr}}^3, \tag{6}$$

since gravity is not acting on the fluid in our simulations.

The integration of Eq. (5) is performed by using an Euler forward integration scheme. Moreover, our lattice-Boltzmann simulations are first-order accurate with respect to time, which is caused by the bounce-back method. Hence applying a higher-order integration scheme would not significantly improve the results.

The simulations were performed on a PC with an AMD Athlon 1800+ processor and 512 MB of memory. Each time step consisted of a propagation step, a collision step, a step for dealing with the static boundaries, two communication steps between the fine and the coarse grid, the calculation of the geometrical quantities of the sphere and the imposition of the moving, no-slip boundary. Each time step costed roughly 5 (s) (wall clock time), hence a typical simulation of 3000 time steps lasted for 4 h. The position and velocity of the sphere was recorded, along with the velocity at one specific position in the flow at $\left(\frac{1}{2}L_x + D_{\mathrm{hydr}}, \frac{1}{2}L_y, D_{\mathrm{hydr}}\right)$. As this position did not per se coincide with the center of some grid cell, the velocity at this position was obtained by linear interpolation of information from adjacent cells. In addition, a snapshot of the flow field was stored when the gap size between the sphere and the bottom amounted to $\delta \approx D_{\mathrm{hydr}}/2$. In the case of $Re_\infty = 1.5$ (S1), also the particle distributions residing on both grids were stored when $\delta/D_{\mathrm{hydr}} \approx 0.5$, together with the corresponding sedimentation velocity W_1. The latter data were used as initial conditions for a more accurate simulation of the bottom part of the trajectory (see the next section).

4.2. Bottom part of the trajectory at $Re_\infty = 1.5$ (simulation S7)

Since the resolution in the previous simulations becomes too coarse when the sphere approaches the bottom of the tank [29], a finer grid is required to resolve the hydrodynamic forces on the sphere more accurately. In general, it is found that for gap sizes larger than roughly 1–2 grid cells, the hydrodynamics can be sufficiently captured [29]. In simulation S7, we therefore continue simulation S1 on an even finer grid for gap sizes $\delta/D_{\mathrm{hydr}} \leqslant 0.5$, corresponding to the sphere positions $z_1 \leqslant D_{\mathrm{hydr}}$ (ls). We introduce four different resolutions rather than two as before in the tank, thereby increasing the resolution between the bottom and the sphere by a factor of 8. This grid setup is shown in Fig. 4 and Table 2. Note that the finest grid completely covers the sphere, so that the sphere does not cross any grid transition interface. Compared to a simulation on a uniform grid with a resolution equal to the resolution of grid G_0, the computational effort (defined as the number of time steps times the number of grid nodes) is now reduced to $C_{\mathrm{refined}}/C_{\mathrm{uniform}} = 0.04\%$, clearly showing the advantage of local grid refinement.

As the resolution of the grid surrounding the sphere becomes eight times higher, so does the resolution of the discretized sphere. Since the hydrodynamic diameter of sphere in simulation S1 amounts to 9.031, the hydrodynamic diameter of the sphere in the present simulation should be eight times larger. In our case, we arrive at a sphere with a hydrodynamic diameter of $D_{\mathrm{hydr}} = 72.95$,

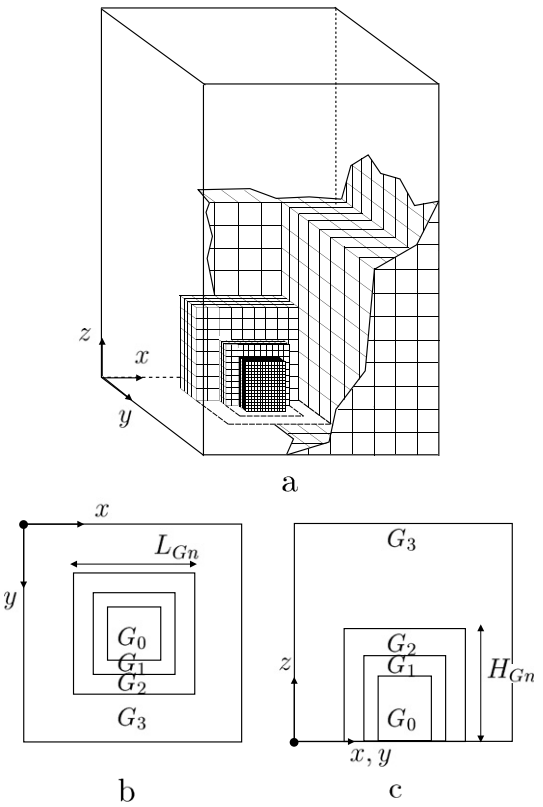

Fig. 4. Grid setup for the bottom part of the sedimentation trajectory of a sphere in a tank, (a) 3D view, (b) top view, and (c) side view. G_0 refers to the finest grid, G_3 to the coarsest grid. The base of each grid is square. The proportions in the figures do not correspond entirely to those in the simulations for clarity reasons.

Table 2
Simulation settings of the bottom part of the sedimentation trajectory of the sphere at $Re_\infty = 1.5$

Quantity	S7
v	$\frac{4}{3}$
W_∞	2.709×10^{-2}
g_z	1.025×10^{-3}
D_{hydr}	72.95
$L_x \times L_y \times L_z$	$480 \times 480 \times 768$
z_1	72.72
W_1	−0.01823
ρ_s/ρ_f	1.155
S	2.056×10^{-4}
T	1.466×10^{-4}

Grid	Resolution	L_{G_n}	H_{G_n}	$\vec{x}_{G_n,0}$
0	$\frac{1}{72}$	80	116	(200, 200, 0)
1	$\frac{1}{36}$	96	124	(192, 192, 0)
2	$\frac{1}{18}$	128	144	(176, 176, 0)
3	$\frac{1}{9}$	480	768	(0, 0, 0)

All quantities are give in lattice-Boltzmann units with respect to the finest grid (i.e. grid G_0).

which is about 1% too large. This hydrodynamic diameter can be obtained with a discretized sphere consisting of 9514 facets, each facet having a size of $\Delta_f \approx 2$. The geometrical diameter then amounts to $D_{\mathrm{geom}} = 75.00$ (ls), which is about 2 (ls) larger than the hydrodynamic diameter. This difference is caused by the relatively large value of the viscosity in lattice-Boltzmann units [1].

The consequence of the high resolution of the grid and the sphere is that in the volumetric no-slip boundary technique, the calculation of the geometrical quantities required for Eq. (3) considerably increases the computational time; after all, for each direction i, the geometrical intersections of all cubic cells near the sphere surface and the triangular prisms have to be calculated first in order to calculate the corresponding volumes. For simulation S7, the calculation of the propagation step, collision step and the communication between two adjacent grids together takes about 10 s on a single AMD Athlon 1800+ processor, whereas the determination of the geometrical quantities for a certain position of the sphere takes 10 min. A simulation of 4000 time steps would therefore last for a month.

The computational time can considerably be reduced by simply calculating the above geometrical quantities of the sphere for a range of positions beforehand. Since the sphere moves in one direction, only positions in the z-direction need to be calculated. In addition, we are only interested in positions of the sphere *relative to the grid*, not positions with respect to the bottom of the tank. The number of positions to be stored is mostly dependent on the gap size (expressed in ls units) between the sphere and the bottom of the tank, because the hydrodynamics in the small gap significantly determines the motion of the sphere. For our simulations, the positions of the sphere in simulation S7 are therefore discretized with spatial steps of $\Delta z = \frac{1}{100}$ (ls). Even for the smallest gap size where the lubrication force can still be captured reasonably well, being roughly 1–2 (ls) on the fine grid, the error with respect to the gap size will then be $\sim \frac{1}{100}$ (ls)/1 (ls) $\times 100\% = 1\%$, which is acceptable for our purposes. Note that the real position of the sphere is derived from the equation of motion and can be *any number*. Once the real position is determined, the sphere is then put onto a pre-processed position (one of the 100 positions in our case) which is closest to the real position.

Since the pre-processed positions relate to a translational motion of the sphere only, the rotational component in the equation of motion is omitted in simulation S7. It was found in simulations S1–S6 that no significant rotation of the sphere took place (angle of rotation $\ll 1°$, results not shown here). It is therefore assumed that the rotation can be left out safely in simulation S7.

Simulation S7 was run on the same machine as simulations S1–S6. The initial flow field was obtained by simply *uniformly* mapping the stored flow field of simulation S1 at $\delta/D_{\mathrm{hydr}} = 0.5$ onto the grid in Fig. 4. This mapping procedure is described by $n_{S7}(\vec{x}_i, t) = n_{S1}(\vec{x}_j, t)$, where $\vec{x}_i$ represents the locations of the eight fine grid cells that are covered by the coarse grid cell at position $\vec{x}_j$. During the simulation, the sedimentation velocity as well as the position of the sphere were recorded for further analysis.

5. Results

5.1. Main trajectory

5.1.1. Experimental uncertainty in Ref. [4]

The experimental uncertainty, which is not given in Ref. [4], is mainly determined by the uncertainty in the viscosity of the fluid (silicone oil) $E_\mu = \pm 1.5\%$ [37] and the uncertainty in the position of the sphere $E_s = \pm 1.5\%$. The total experimental uncertainty in the sedimentation velocity amounts to

$$\frac{\Delta W}{W} \approx \pm (E_\mu^2 + E_s^2)^{1/2} = \pm 3.2 - 3.5\%$$

for the cases studied in this work. Details can be found in Ref. [38].

5.1.2. Velocity field at $\delta/D_{\mathrm{hydr}} = 0.5$ and $y = L_y/2$

The first results refer to a qualitative comparison of the flow fields obtained from the experiments and simulations S1 and S4 at $\delta/D_{\mathrm{hydr}} = 0.5$ and $y = L_y/2$ (for brevity, S2 and S3 are omitted). The vector fields and contour plots are shown in Fig. 5. The figure clearly shows that our simulations agree well with the experiments. The difference between our results and the simulations of ten Cate et al. is most profound for $Re_\infty = 1.5$, the other simulation (S4 and also S2 and S3) show quite similar results. For $Re_\infty = 1.5$, the simulation of ten Cate et al. underpredicts the velocities around the sphere.

It should be noticed that the post-processing step, as denoted in Ref. [3], is not applied here, since the fluctuations,

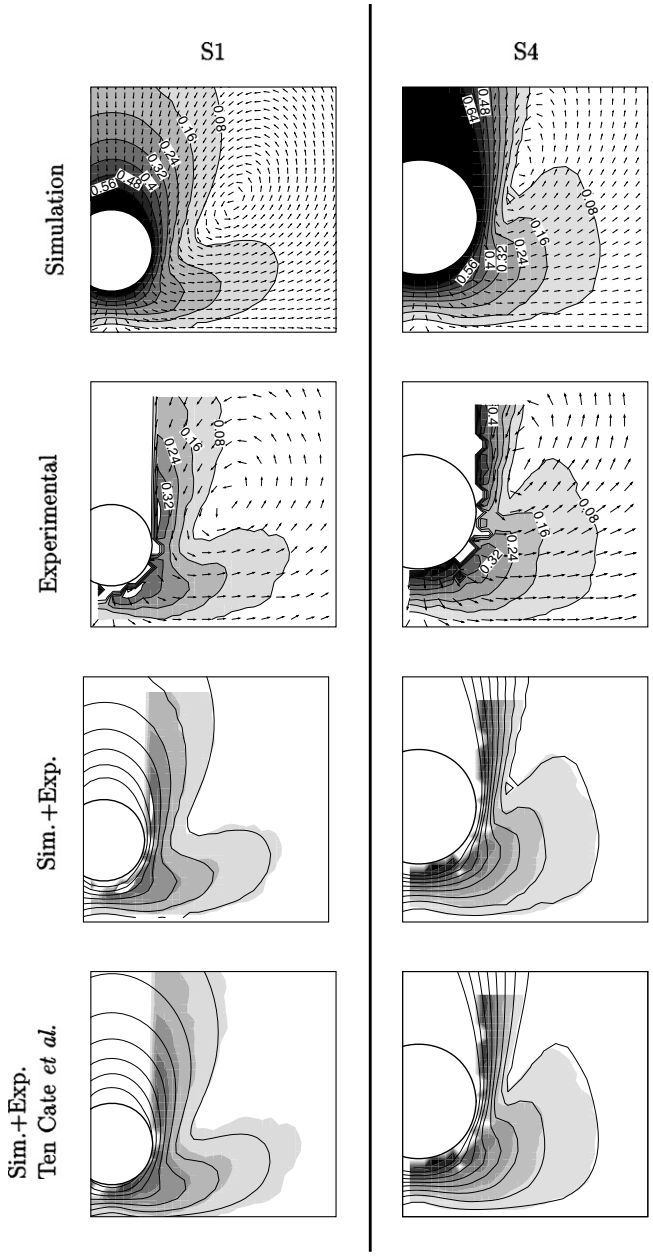

Fig. 5. Contour and vector plots of our simulated flow field (S1 and S4), of the experimentally obtained flow field, of our simulations combined with the experiments and of the simulations of ten Cate et al. combined with the experiments. The gap size amounts to $\delta/D_{\mathrm{hydr}} = 0.5$ and $y = L_y/2$, the contour lines refer to the dimensionless velocity $|\vec{u}|/W_\infty$. The vectors represent the direction of the flow only.

induced by the grid refinement technique, are found to be very small. Such fluctuations, however, do exist in the flow and will be studied later in this section.

5.1.3. Sedimentation velocity and position of the sphere

The sedimentation velocity versus the position of the sphere is shown in Fig. 6. Note that the velocity and position are not plotted versus time, so that the error due to the time offset for each separate time series in Ref. [4] can be

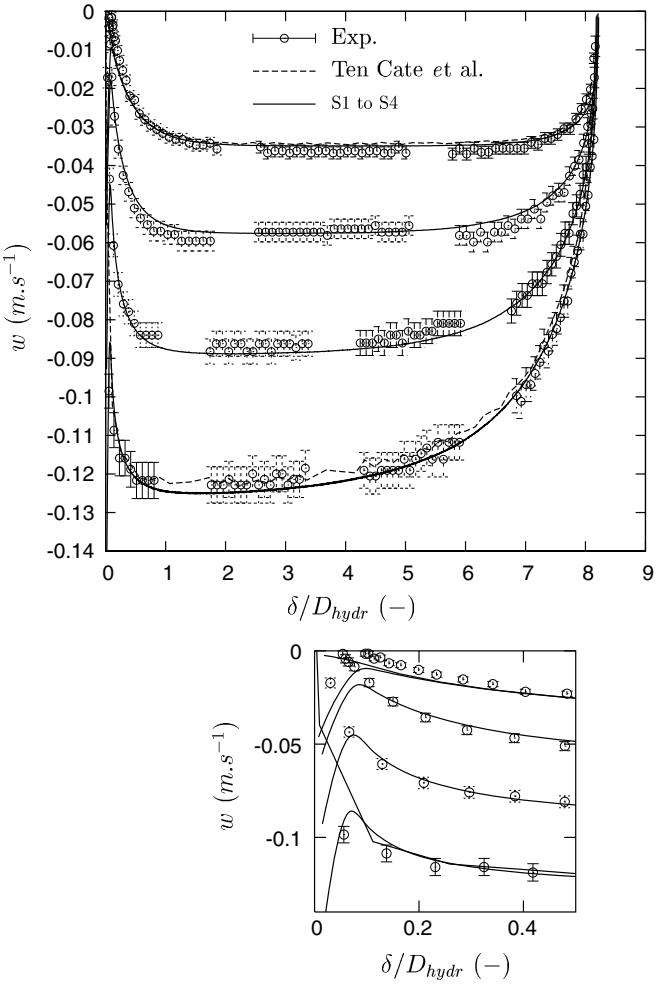

Fig. 6. Sedimentation velocity versus the dimensionless gap size δ/D_{hydr} for simulations S1–S4, compared to the simulation and experimental results from ten Cate et al. [4] (Only the simulations for $Re_\infty = 1.5$ and 31.9 are given by ten Cate et al.). The lower plot shows a detail of the upper plot.

avoided. The figure shows that all our simulation results mostly fall within the experimental error.

The deviation between the experiments and simulation S1 is approximately 3.5%, which is just within the error interval of the experimental data. For S2, the agreement is good for the steady-state part of the trajectory, but the acceleration and deceleration parts slightly deviate from the experiments. As, however, the measurements themselves show a discontinuous profile, we consider S2 to be less suitable for a quantitative comparison. The agreement between the experiments and simulations S3 and S4 all fall within the error interval of the experimental data.

It is quite remarkable that the results of simulations S3 and S4 are even better than for S1 and S2, since the hydrodynamic diameter is calibrated with the help of Hasimoto's Stokes flow benchmark case [36]. These results seem to indicate (not prove) that the error caused by the volumetric boundary technique is dependent on the viscosity as well as on the resolution, but not on the specific character of the

flow itself. Such an issue, however, needs to be studied more extensively.

As the sphere approaches the bottom of the tank, the resolution in the gap becomes too coarse to resolve the lubrication force accurately. For very small gap sizes, unphysical sedimentation velocities are therefore to be expected. Fig. 6 indeed shows a sudden increase in the sedimentation velocity for gapsizes $\delta/D_{\mathrm{hydr}} \to 0$.

The simulation data of ten Cate et al. are also included in Fig. 6, showing that these data also fall within the error interval of the experimental data. From Fig. 6, we clearly can see fluctuations in the sedimentation velocity, introduced by the adaptive forcing technique for moving boundaries applied in Ref. [4]. This technique uses internal grid nodes, which, as already mentioned earlier in this work, cause fluctuating and unstable behaviour for freely moving boundaries at low solid-to-fluid density ratios. Such fluctuations do not occur in our simulations, since the volumetric boundary technique lacks the use of internal grid nodes.

5.1.4. Time series at one specific position

The time series of the velocities at one specific location (i.e. sample point) in the flow at $\left(\frac{1}{2}L_x + D_{\mathrm{hydr}}, \frac{1}{2}L_y, D_{\mathrm{hydr}}\right)$ are shown in Figs. 7 and 8. This point is chosen to be near the center of the moving, trailing vortex, where large changes in the local velocities occur during the sedimentation of the sphere. Our simulations as well as the experimental data of ten Cate et al. are included in the figure. In addition, the simulation results for $Re_\infty = 1.5$ and $Re_\infty = 31.9$ of ten Cate et al. are shown in order to examine the effect of using different lattice-Boltzmann techniques (the other two Reynolds numbers are not shown in Ref. [4]). The hydrodynamic diameters in those simulations are close to ours, and amount to $D_{\mathrm{hydr}} = 8.974$ (ls) and $D_{\mathrm{hydr}} = 9.620$ (ls), respectively.

For all Reynolds numbers, our simulation results agree well with the experimental data. The largest deviations can be found for S2, where the peaks of the simulated velocities show slightly smaller values than in the experiments. Considering the time scale, however, all peaks are captured accurately. The time instants and widths of the peaks are resolved quite well for all Reynolds numbers. It is interesting to note that the sample point is located on the *coarse* grid and near the grid transition interface. Hence, in spite of the resolution of the coarse grid, accurate results can be obtained.

Each sub-figure in Figs. 7 and 8 contains two sharp peaks with opposite direction. These peaks originate from not applying a model for the lubrication force as the sphere approaches the bottom of the tank. As explained

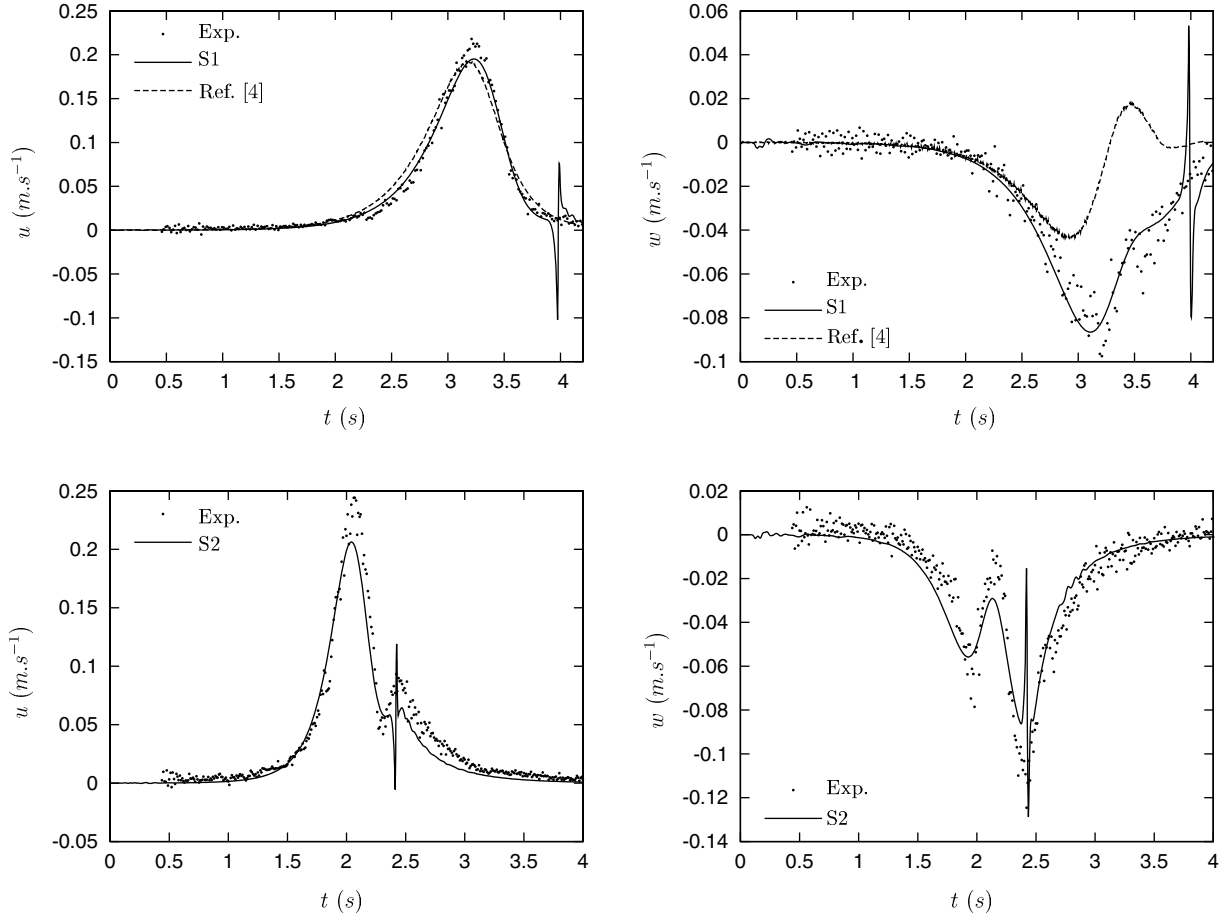

Fig. 7. Time series of the velocities at a sample point located at $\left(\frac{1}{2}L_x + D_{\mathrm{hydr}}, \frac{1}{2}L_y, D_{\mathrm{hydr}}\right)$ for S1 and S2.

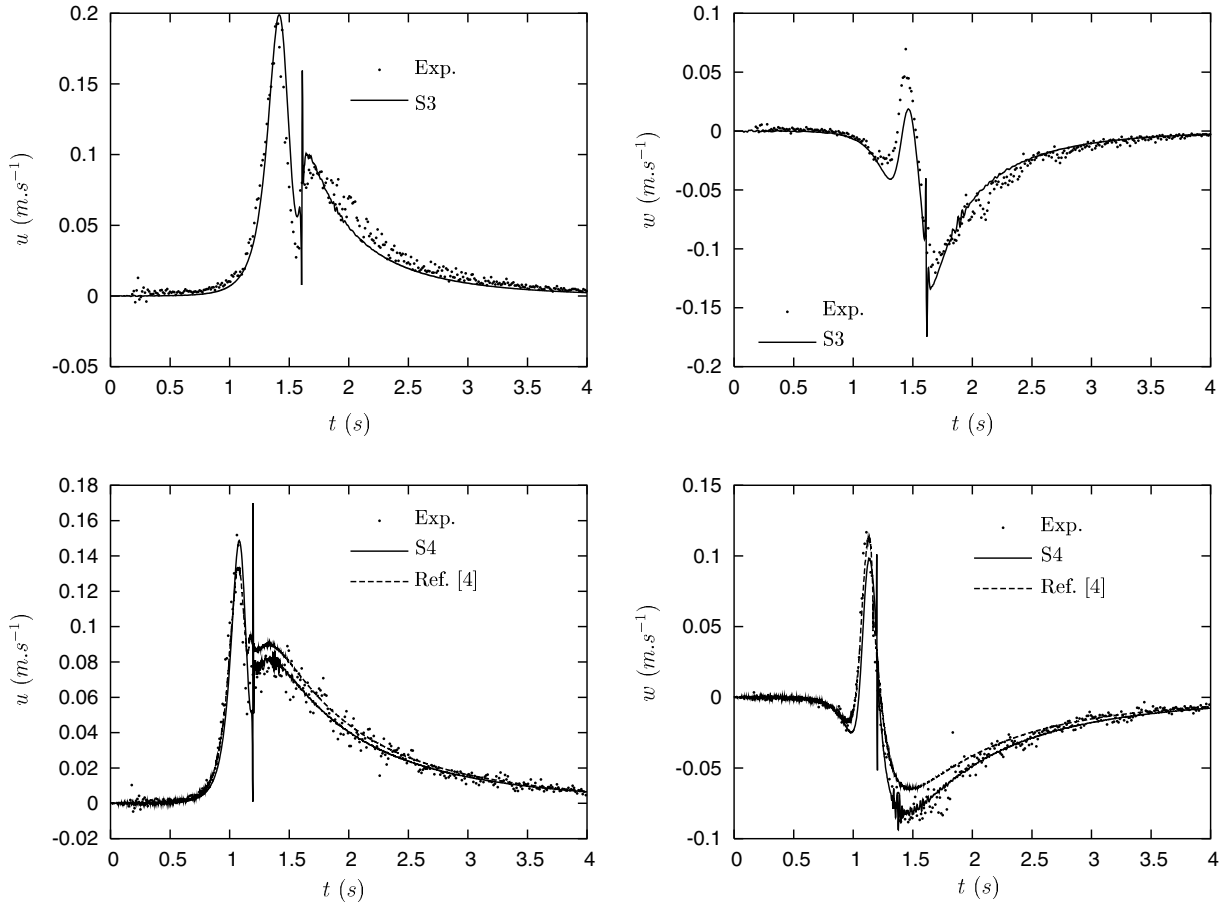

Fig. 8. Time series of the velocities at a sample point located at $\left(\frac{1}{2}L_x + D_{\text{hydr}}, \frac{1}{2}L_y, D_{\text{hydr}}\right)$ for S3 and S4.

previously, the strong lubrication force cannot be captured accurately when $\delta < 2$ (ls), which results in a sudden, non-physical increase of the sphere's sedimentation velocity. These two peaks, however, do not seem to be of much influence on the flow field in the subsequent time steps.

The time series show that the simulations in this work capture the velocities more accurately than the uniform grid simulations performed by ten Cate et al., even though a coarser grid has been used in the larger part of the tank in our case. Especially at $Re_\infty = 1.5$, the differences between both simulations are quite pronounced, which is in accordance with the results shown in Fig. 5. We think that these differences are mainly caused by the use of a different technique for the moving no-slip boundary. One could argue that a different lattice-Boltzmann scheme may also cause deviations,[1] but the scheme due to Somers is algebraically practically similar to an 18-speed LBGK scheme in the case of low Reynolds number flows.

[1] ten Cate et al. used the scheme due to Somers [28] instead of the LBGK scheme.

5.1.5. Simulation at $Re_\infty = 1.5$ for a solid-to-fluid density ratio close to 1

Several existing lattice-Boltzmann techniques for moving boundaries use *internal grid nodes* (i.e. grid nodes inside the moving object), such as the techniques as described in Refs. [4,17]. The advantage of such an approach is that no additional algorithm is needed for grid nodes that disappear or reappear due to the motion of the object. The inclusion of internal grid nodes introduces additional inertia to the particle, for which a correction must be included in the equation of motion [17]. This additional term, however, leads to instabilities for low solid-to-fluid density ratios. Lowe et al. [21] proposed an implicit integration scheme, which showed to be unconditionally stable. Such an implicit scheme is computationally slightly more demanding since six coupled equations (for each translational and rotational velocity component) need to be solved and two separate sweeps through all boundary grid nodes are required. Aidun et al. [39] excluded the internal grid nodes, thereby using staircase shaped surfaces. Indeed, no instabilities were found in [39].

Since no internal grid nodes or grid cells are needed in the volumetric technique for moving no-slip boundaries, the widely experienced problem of instabilities induced by a solid-to-fluid density ratio close to 1 is absent. This can

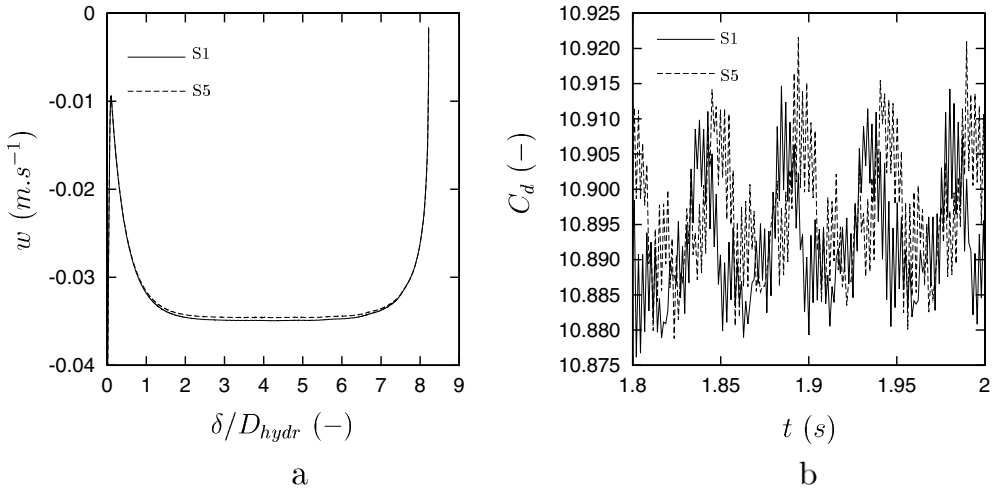

Fig. 9. Sedimentation velocity versus position (a) and the dimensionless hydrodynamic force $F_{fp,z}/\left(\frac{1}{2}\rho W^2 \cdot \frac{1}{4}\pi D_{\mathrm{hydr}}^2\right)$ acting on the sphere (b) for simulations S1 and S5.

be shown by comparing the results of simulation S5 (density ratio $\rho_s/\rho_f = 1.01$) with the results of simulation S1 ($\rho_s/\rho_f = 1.155$). In order to fix the Reynolds number to $Re_\infty = 1.5$, we therefore increase gravity and, by doing so, avoid adjusting other parameters such as the resolution or the viscosity (hydrodynamic diameter). The settings for S5 can be found in Table 1.

The sedimentation velocity versus the position of the sphere for S1 and S5 is shown in Fig. 9a. It is found that the difference between the velocities of both simulations is very small, which should be the case for the stationary part of the trajectory (This is not the case when $du/dt \neq 0$, as the acceleration (and deceleration) of the sphere is different for S1 and S5 due to the different masses of the sphere). In addition, and more important, instabilities do not occur in spite of the explicit, Euler forward integration scheme for the equation of motion of the sphere. We can investigate such unstable behaviour by monitoring the hydrodynamic force $\vec{F}_{\mathrm{fp}}$ acting on the sphere; if the force is strongly fluctuating in time, and these fluctuations significantly increase in amplitude as the density ratio goes to 1, instabilities may occur. In the present simulations, however, the fluctuations are found to be very small (<0.1%) and do not grow as the density ratio is decreased from 1.155 to 1.010 (see Fig. 9b).

5.1.6. Interpolated versus uniform redistribution of particle densities for the volumetric boundary technique

Simulations on 2D laminar channel flow revealed that the accuracy of the volumetric boundary method can be improved by applying an interpolation on the particle densities involved [1]. We can further investigate the implications of such an interpolation for a *freely moving* boundary by repeating simulation S1 with a *uniform* redistribution of particle densities (S6). The sedimentation velocity versus the position of the sphere is shown in Fig. 10 for both simulations, as well as the experimental data of ten Cate et al.. The figure indicates that the sphere

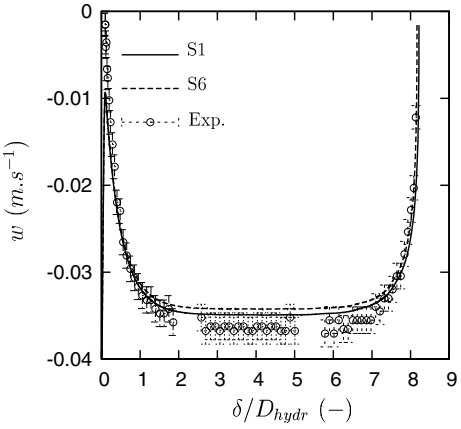

Fig. 10. Sedimentation velocity versus position for simulations S1 and S6.

sediments with a lower velocity when a uniform redistribution of particle densities is applied. The deviation between the experiments and simulation S6 is now 5.5%, being 2% larger than the deviation found in simulation S1. These findings therefore (again) indicate that the accuracy of the volumetric boundary technique can also be improved through interpolation of particle densities in the case of a moving boundary.

5.1.7. Hydrodynamic temporal and spatial fluctuations

In Ref. [3], it was found that, in contrast to methods described in e.g. Refs. [10,12–16], the local grid refinement technique introduces temporal and spatial velocity fluctuations on the fine grid. Since these fluctuations are related to velocities normal to the grid transition interface, we would therefore expect such fluctuations in the x- and y-directions for a grid setup as shown in Fig. 2; hence, a fluctuating u-velocity in the x-direction and a fluctuating v-velocity in the y-direction. The velocities in three directions for $Re_\infty = 31.9$ (simulation S4) are shown in Fig. 11.

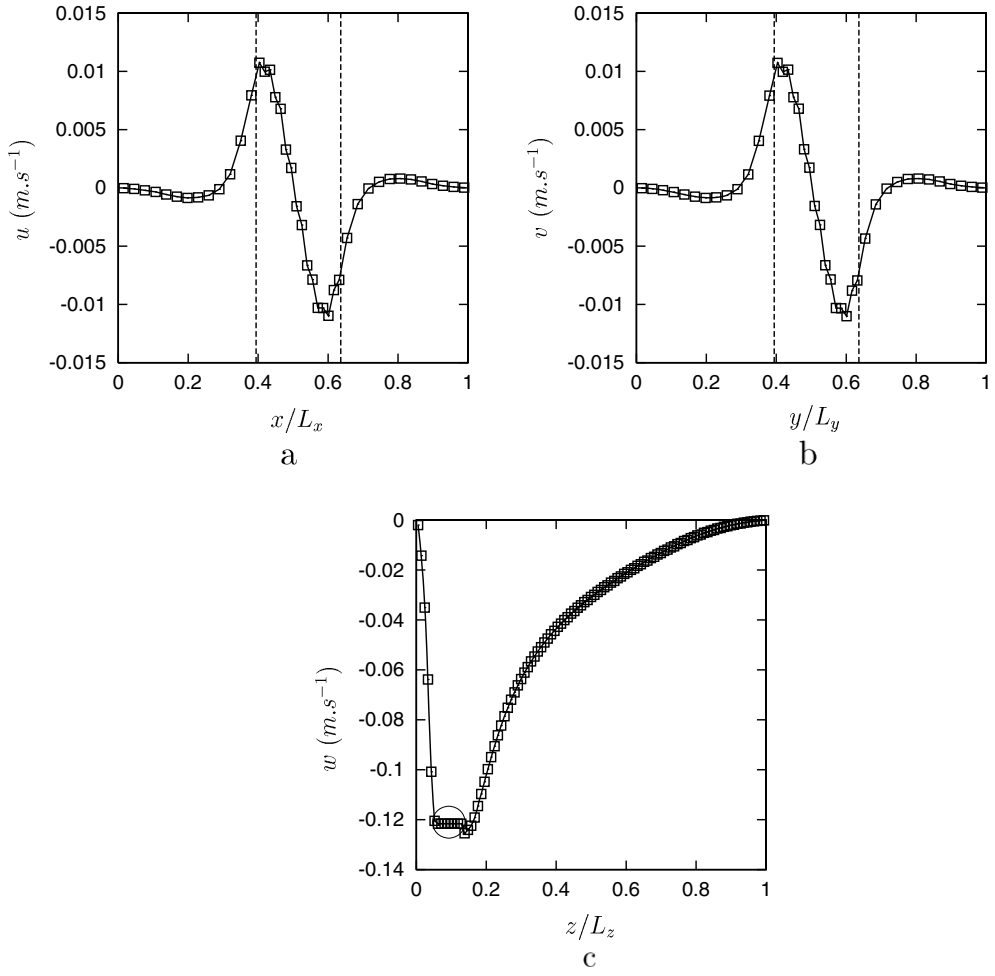

Fig. 11. Velocities in the tank in the three directions at $Re_\infty = 31.9$ (S4) at a gap size of $\delta/D_{\text{hydr}} = 0.50$: (a) u-velocity for $y/L_y \approx 0.5$ and $z/L_z \approx 0.19$, (b) v-velocity for $x/L_x \approx 0.5$ and $z/L_z \approx 0.19$ and (c) w-velocity for $x/L_x \approx 0.5$ and $y/L_y \approx 0.5$ (position of the sphere is indicated). The dashed lines represent the grid transition interfaces. Note that the finest grid in S4 is not located in the center of the tank.

As expected, the velocities in the x- and y-directions exhibit small fluctuations, though hardly visible. No fluctuations are detected in the z-direction, as these velocities are parallel to the grid transition interfaces. No significant influence of the fluctuations on the simulations is found, which can be explained by the small amplitude of the fluctuations and the small time scale of the staggering with respect to the time scales present in the flow, denoted by the ratio of both time scales $\Delta t_{\text{fluctuations}}/\Delta t_{\text{flow}} = 1/(D_{\text{hydr}}/W_\infty) \ll 1$.

5.2. Bottom trajectory at $Re_\infty = 1.5$

5.2.1. Time series of the flow field close to the bottom

With the help of the local grid refinement, we are capable of examining the flow field close to the bottom in more detail. We therefore plot a time series of the flow field for gap sizes in the range of $0.025 < \delta/D_{\text{hydr}} < 0.20$ (see Fig. 12) with a time interval of 0.12 (s). From the figure, we can see that from $t = 3.88$ (s), velocities higher than the sedimentation velocity can be found between the sphere and the bottom of the tank. As the gap becomes smaller, so does the surface through which the fluid is squeezed from the gap into the bulk of the tank, which apparently results in a strong local increase in the velocity of the fluid.

5.2.2. Sedimentation velocity and position of the sphere

The sedimentation velocity of the sphere close to the bottom, i.e. $\delta/D_{\text{hydr}} < 1$, is plotted versus the dimensionless gap size in Fig 13. Before the results will be analyzed, it should be noted that in the experimental data, a small gap δ_∞ remains between the sphere and the bottom of the tank as the sedimentation velocity already amounts to zero. This remaining gap is very small compared to the total length of the sedimentation trajectory (i.e. $\delta_\infty/z_0 = 0.01$), but obviously becomes significant when processes close to the bottom are considered. After analyzing the experimental data carefully and taking the negligible error in the position of the sphere into account, however, we think that we may safely shift the measured

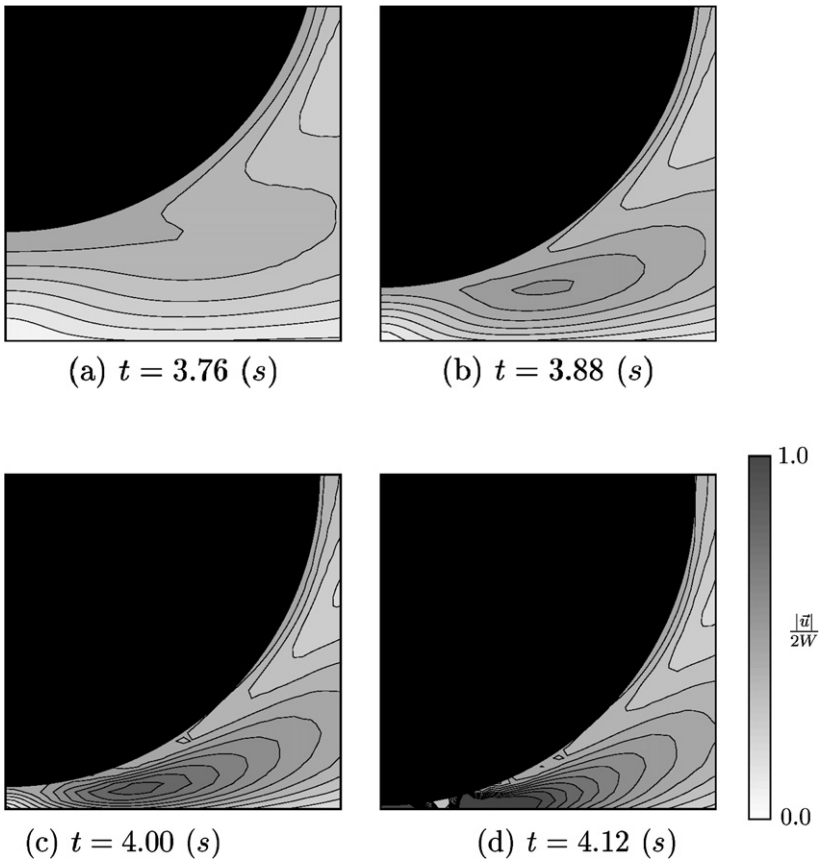

Fig. 12. Detailed view of the velocity field in the gap between the sphere and the bottom of the tank at $Re_\infty = 1.5$. Note that the dimensionless velocity at the surface of the sphere amounts to $|\vec{u}|/(2W) = \frac{1}{2}$.

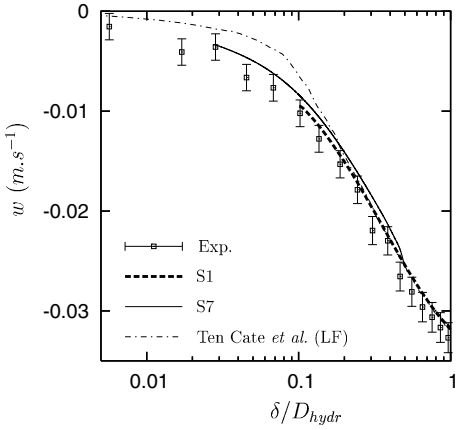

Fig. 13. The sedimentation velocity versus the position of the sphere close to the bottom of the tank for simulations S1 and S7, together with the simulation and experimental data from ten Cate et al. [4]. The suffix 'LF' denotes a simulation where a model for the lubrication force has been applied.

position such that the sphere touches the bottom as the sedimentation velocity is zero, hence $\delta \to \delta - \delta_\infty$.

Fig. 13 clearly shows that the sedimentation velocity and trajectory close to the bottom can now be calculated even for gap sizes in the range of $0.02 < \delta/D_{\text{hydr}} < 0.1$, which was not possible with the grid setup in simulation S1. Moreover, the results of simulation S7 are in good agreement with the experiments. The sedimentation velocities of simulation S7 are found to be slightly smaller than the velocities found in simulation S1, caused by a hydrodynamic force per surface unit being a little larger in S7 than in S1. Nevertheless, since the difference between both simulations is small, this issue has not been studied in further detail.

It should be noted here that for gap sizes smaller than roughly 1–2 (ls) (i.e. $\delta/D_{\text{hydr}} < 0.02$), the results become non-physical. A similar phenomenon was observed in simulation S1 and is related to the lack of resolution in the gap (see e.g. Fig. 6). Moreover, as the geometrical diameter of the sphere is about 2 ls larger than the hydrodynamic diameter (see Section 4.2), some facets of the sphere would intersect with the bottom of the box. Hence, if one is interested in examining the hydrodynamics for even smaller gap sizes, the grid should be refined *ad infinitum* according to lubrication theory.

Fig. 13 also comprises the results of a simulation of ten Cate et al., where a model for the lubrication force has been used for gap sizes $\delta/D_{\text{hydr}} < 0.14$. The sedimentation velocities of their simulation are practically similar to those of simulation S1 for gap sizes $\delta/D_{\text{hydr}} > 0.14$, but the velocities are clearly underestimated for smaller gap sizes.

6. Conclusion

The applicability of several lattice-Boltzmann techniques for the no-slip boundary condition and local grid refinement has been examined by applying them to the case of a sedimenting sphere in a square based tank. This flow problem covers several physical and numerical issues of interest, such as a freely moving boundary and the presence of multiple temporal and spatial scales, implying the need for locally refined grids. The results from the lattice-Boltzmann simulations performed here have been compared with experimental and numerical data as described by ten Cate et al. in Ref. [4]. Flow field properties as well as the sedimentation velocity and position of the sphere in the tank, have been used for such comparison.

The simulations revealed that the volumetric method for moving boundaries as well as our local grid refinement technique are capable of simulating the flow problem of the sedimenting sphere accurately. Flow field properties, such as the velocity field close to the bottom and the time series of the velocity at one specific point in the flow were in good agreement with the experimental data, even for solid-to-fluid density ratios close to one.

In the future, the volumetric boundary technique needs to be extended, such that moving surfaces can *cross* grid transition interfaces. In our case of the sphere approaching the bottom of the tank, for example, such extensions would very much decrease the computational effort and increase the effectiveness of the local grid refinement technique.

References

[1] Rohde M, Derksen JJ, van den Akker HEA. Volumetric method for calculating the flow around moving objects in lattice-Boltzmann schemes. Phys Rev E 2002;65:056701.

[2] Rohde M, Kandhai D, Derksen JJ, van den Akker HEA. Improved bounce-back methods for no-slip walls in lattice-Boltzmann schemes: theory and simulations. Phys Rev E 2003;67:066703.

[3] Rohde M, Kandhai D, Derksen JJ, van den Akker HEA. A generic, mass conservative local grid refinement technique for lattice-Boltzmann schemes. Int J Num Meth Fluids 2006;54(1):439–68.

[4] ten Cate A, Nieuwstad CH, Derksen JJ, van den Akker HEA. PIV measurements and lattice-Boltzmann simulations on a single sphere settling under gravity. Phys Fluids 2002;14(11):4012–25.

[5] Derksen JJ, van den Akker HEA. Large Eddy simulations on the flow driven by a Rushton turbine. AIChE J 1999;45(2):209–21.

[6] Derksen JJ, van den Akker HEA. Simulation of vortex core precession in a reverse-flow cyclone. AIChE J 2000;46(7):1317–36.

[7] Hartmann H, Derksen JJ, Montavon C, Pearson J, Hamill IS, van den Akker HEA. Assessment of large Eddy and RANS stirred tank simulations by means of LDA. Chem Eng Sci 2004;59(12):2419–31.

[8] Freund H, Zeiser T, Huber F, Klemm E, Brenner G, Durst F, et al. Numerical simulations of single phase reacting flow in randomly packed fixed-bed reactors and experimental validation. Chem Eng Sci 2003;58:903–10.

[9] Fares E. Unsteady flow simulation of the ahmed reference body using a lattice-Boltzmann approach. Comp Fluids 2006;35:940–50.

[10] Filippova O, Hänel D. Boundary-fitting and local grid refinement for lattice-bgk models. Int J Mod Phys C 1998;9(8):1271–9.

[11] Lin C, Lai YG. Lattice Boltzmann method on composite grids. Phys Rev E 2000;62(2):2219–25.

[12] Dupuis A, Chopard B. Theory and applications of an alternative lattice-Boltzmann grid refinement algorithm. Phys Rev E 2003;67:066707.

[13] Crouse B, Rank E, Krafczyk M, Tölke J. A LB-based approach for adaptive flow simulations. Int J Mod Phys B 2002;17:109–12.

[14] Yu D, Mei R, Shyy W. A multi-block lattice-Boltzmann method for viscous fluid flows. Int J Num Meth Fluids 2002;39(2):99–120.

[15] Rheinländer M. A consistent grid coupling method for lattice-Boltzmann schemes. J Stat Phys 2005;121(1–2):49–74.

[16] Tölke J, Freudiger S, Krafczyk M. An adaptive scheme using hierarchical grids for lattice-Boltzmann multi-phase flow simulations. Comp Fluids 2006;35(8–9):820–30.

[17] Ladd AJC. Numerical simulation of particulate suspensions via a discretized Boltzmann Equation. Part I. Theoretical foundation. J Fluid Mech 1994;271:285–309.

[18] Verberg R, Ladd AJC. Lattice-Boltzmann model with sub-grid-scale boundary conditions. Phys Rev Lett 2000;84(10):2148–51.

[19] Bouzidi M, Firdaouss M, Lallemand P. Momentum transfer of a Boltzmann-lattice fluid with boundaries. Phys Fluids 2001;13(11):3452–9.

[20] Ginzburg I, d'Humières D. Multireflection boundary conditions for lattice-Boltzmann models. Phys Rev E 2003;68:066614.

[21] Lowe CP, Frenkel D, Masters AJ. Long-time tails in angular momentum correlations. J Chem Phys 1995;103(4):1582–7.

[22] Ladd AJC. Numerical simulation of particulate suspensions via a discretized Boltzmann equation. Part II. Numerical results. J Fluid Mech 1994;271:311–39.

[23] Pagonabarraga I, Hagen MHJ, Lowe CP, Frenkel D. Short-time dynamics of colloidal suspensions in confined geometries. Phys Rev E 1999;59(4):4458.

[24] Nguyen N, Ladd A. Sedimentation of hard-sphere suspensions at low Reynolds number. J Fluid Mech 2005;525:73–104.

[25] Ding E, Aidun C. Extension of the lattice-Boltzmann method for direct simulation of suspended particles near contact. J Stat Phys 2003;112(3–4):685–708.

[26] Feng Z, Michaelides E. Proteus: a direct forcing method in the simulations of particulate flows. J Comp Phys 2005;202:20–51.

[27] Pianet G, ten Cate A, Derksen J, Arquis E. Assessment of the 1-fluid method for dns of particulate flows: sedimentation of a single sphere at moderate to high reynolds numbers. Comp Fluids 2007;36:359–75.

[28] Somers JA. Direct simulation of fluid flow with cellular automata and the lattice-Boltzmann equation. Appl Sci Res 1993;51:127–33.

[29] Ladd AJC, Verberg R. Lattice-Boltzmann simulations of particle-fluid suspensions. J Stat Phys 2001;104(5/6):1191–251.

[30] Ladd AJC. Dynamics: models and kinetic methods for non-equilibrium many body systems. Dordrecht: Kluwer Academic Publishers; 2000.

[31] Cao N, Chen S, Jin S, Martinez D. Physical symmetry and lattice symmetry in the lattice-Boltzmann method. Phys Rev E 1997;55:R21–4.

[32] Chen H, Teixeira C, Molvig K. Realization of fluid boundary conditions via discrete Boltzmann dynamics. Int J Mod Phys C 1998;9(8):1281.

[33] He X, Zou Q, Luo L, Dembo M. Analytic solutions and analysis on non-slip boundary conditions for the lattice-Boltzmann BGK model. J Stat Phys 1997;87(1–2):115.

[34] d'Humières D, Ginzburg I, Krafczyk M, Lallemand P, Luo L. Multiple-relaxation-time lattice-Boltzmann models in three dimensions. Phil Trans R Soc Lond A 2002;360(1792):437–51.

[35] Pan C, Luo L, Miller CT. An evaluation of lattice-Boltzmann schemes for porous medium flow simulations. Comp Fluids 2006;35:898–909.

[36] Hasimoto H. On the periodic fundamental solutions of the stokes equations and their application to viscous flow past a cubic array of spheres. J Fluid Mech 1959;5:317–28.

[37] Nieuwstad CH, P.I.V. experiments on the flow induced by a sphere sedimenting towards a solid wall. Master's thesis. The Netherlands: Delft University of Technology; 2001.
[38] Rohde M. Extending the lattice-Boltzmann method: novel techniques for local grid refinement and boundary conditions. Ph.D. thesis. The Netherlands : Delft University of Technology, download from <www.library.tudelft.nl/>; 2004.
[39] Aidun CK, Lu Y, Ding EJ. Direct analysis of particulate suspensions with inertia using the discrete Boltzmann equation. J Fluid Mech 1998;373:287–311.